Z. angew. Math. Phys. 52 (2001) 33–61
0044-2275/01/010033-29 $ 1.50+0.20/0

Zeitschrift für angewandte Mathematik und Physik ZAMP

The oscillatory channel flow with arbitrary wall injection

Joseph Majdalani

Abstract. In this article, we consider the laminar oscillatory flow in a low aspect ratio channel with porous walls. For small-amplitude pressure oscillations, we derive asymptotic formulations for the flow parameters using three different perturbation approaches. The undisturbed state is represented by an arbitrary mean-flow solution satisfying the Berman equation. For uniform wall injection, symmetric solutions are obtained for the temporal field from both the linearized vorticity and momentum transport equations. Asymptotic solutions that have dissimilar expressions are compared and shown to agree favourably with one another and with numerical experiments. In fact, numerical simulations of both linearly perturbed and nonlinear Navier-Stokes equations are used for validation purposes. As we insist on verifications, the absolute error associated with the total time-dependent velocities is analysed. The order of the cumulative error is established and the formulation based on the two-variable multiple-scale approach is found to be the most general and accurate. The explicit formulations help unveil interesting technical features and vortical structures associated with the oscillatory wave character. A similarity parameter is shown to exist in all formulations regardless of the mean-flow selection.

Mathematics Subject Classification (1991). 76N20, 34E10, 76D30, 35D99, 34E99.

Keywords. Oscillatory flow, porous walls, multiple scales, WKB, asymptotic expansions.

1. Introduction

A problem that has become a classic in fluid mechanics is the study of laminar flows in channels with porous walls. Over the past four decades, numerous analytical and numerical investigations have, in fact, been devoted to derive exact or approximate mean-flow solutions in the presence of different ranges of cross-flow Reynolds numbers. A number of experimental investigations have also been conducted for validation purposes. Reported results have indicated the presence of rich structures and intellectually challenging flow features depending on the assumptions used, initial conditions, and injection levels.

For suction at the porous surface, inflection points were often detected in some ranges of the cross-flow Reynolds number R. These points heralded solution multiplicity and possible flow reversal and instability. Conversely, wall injection promoted unique solutions that became more stable to temporal disturbances with

successive increases in R. The existence of single or dual solutions was first assessed numerically, and later proved rigorously by a group of capable mathematicians.

In principle, most theoretical investigations in channels with porous walls have relied on steady mainstream formulations based on an exact similarity solution that was presented by Berman [1]. In fact, assuming a streamfunction that varied linearly with the axial coordinate, Berman was able to collapse the Navier-Stokes equations into a single, nonlinear, fourth-order differential equation. The latter depended on four boundary conditions and a Reynolds number R. This so-called cross-flow Reynolds number was based on the wall injection speed v_w, channel half-spacing h, and viscosity ν. Except for infinitely large R, Berman's differential equation precluded the attainment of exact analytical solutions in finite form. Historically, asymptotic series expansions and numerical simulations were initiated in concert to obtain solutions over various ranges of R. Examples abound and some will be briskly revisited to gain perspective on the problem at hand.

In 1953, Berman managed a regular perturbation expansion in R that became asymptotically exact as $R \to 0$. This was followed by a first-order approximation by Sellars [2] who addressed the large suction case. For infinitely large injection, Taylor [3] exacted an elegant formulation that has come to be known as the Taylor flow. Taylor's solution coincided with the leading-order term of an expansion for $R \gg 0$ that was carried out, totally independently, by Yuan [4].

In an attempt to cover the entire injection range, Morduchow [5] employed numerical curve-fitting concepts to contrive nonunique, user-defined approximations. In the same vein of achieving greater uniformity, White et al. [6] produced a convergent power series that was applicable to an arbitrary R. The generality of the latter was offset by the need to calculate the power series coefficients iteratively. An era of improvements and refinements followed subsequently.

Archetypal examples are found in Terrill [7] who enhanced Sellars's earlier expansion by reproducing additional terms for large suction. He also extended Berman's series for $R \to 0$. In order to remove a singularity occurring in Yuan's large injection formula, Terrill [8] introduced exponentially small terms in association with matched asymptotic expansions to capture the inner layer near the core.

The main focus was later shifted to consider spatial instabilities that were exceptionally pronounced in the event of fluid withdrawal at the porous surface. Works included those by Varapaev and Yagodkin [9], Raithby and Knudsen [10], Brady [11], and Durlofsky and Brady [12]. Almost invariably, the onset of instability was associated with the presence of inflection points and multiple solutions. The issue of solution multiplicity was addressed, in turn, by a number of authors. These included Robinson [13], Skalak and Wang [14], Shih [15], Hastings et al. [16], Lu et al. [17], MacGillvray and Lu [18], and Lu [19]. When injection was concerned, Skalak and Wang [14] reported unique and stable solutions. The corresponding proof was carried out by both Shih [15] and Hastings et al. [16].

Sporadic studies continued to appear in the literature. The temporal stability

of channel flows with porous walls also received attention vis-à-vis the works of Zaturska et al. [20], Taylor et al. [21], and Watson et al. [22]. Such studies confirmed that steady symmetric flows of the injection type were stable to time-dependent perturbations.

The level of complexity is raised considerably when the steady mainstream solution to Berman's equation is subjected to small-amplitude pressure perturbations. From a practical standpoint, it is inevitable that time-dependent fluctuations will occur during the injection process. The ensuing acoustic environment will thus exhibit small amplitude pressure oscillations. Since no former theoretical treatment seems to have addressed the resulting temporal solution, it is the purpose of this article to develop a general model for oscillatory flows that are bounded by permeable surfaces.

The onset of harmonic pressure oscillations can occur in a number of engineering applications. Examples include filtration, phase sublimation, surface ablation, propellant combustion, biological transport in living organisms, and chemical dispensing through porous media. The source of harmonic waves can be external, user-defined, or internal, decreed by the channel's natural frequency. An example of the former type has been achieved in long rectangular channels by Ma et al. [23], [24], and Barron et al. [25]. These were motivated by the need to simulate the burning process of solid propellant grains in a hazard-free environment. To that end, both Ma and Barron constructed cold-flow facilities that comprised sections where sublimating carbon dioxide could originate from flat rectangular blocks. The sublimating sections thus emulated transpiring walls along which gases could be expelled into the channel. Wave generation was accomplished by means of electric motors harnessed to either a slider-crank or a Scotch-yoke mechanism. Naturally, the to-and-fro piston motion caused the injectant to vibrate harmonically at user-controlled frequencies.

The establishment of self-excited pressure oscillations has been recently described by Avalon et al. [26], and Casalis et al. [27]. Their facility used air as the working fluid inside a long channel with counterfacing permeable and impermeable walls. Inevitably, small fluctuations in the injection rate triggered a strong acoustic environment that depended on the system geometry. In all three experiments cited above, the placement of a choked orifice or nozzle at the channel's downstream end caused the oscillation mode character to be of the closed-closed type. The forthcoming model will therefore be tailored to incorporate such oscillation mode shapes. It is hoped that the resulting formulations will be useful in predicting the temporal field arising in physical settings whose mainstream can be described by one of Berman's mean flow solutions.

The strategy we follow is well-conceived. In section 2, we define the geometry and Berman's mainstream solution. Fundamental criteria that justify a perturbation scheme are also visited. In section 3, we exploit the small injection Mach number and normalized pressure wave amplitude to derive a linearized set of Navier-Stokes equations. The velocity vector is subsequently decomposed, in

section 4, into irrotational and solenoidal parts. This allows splitting the linearized equations into two distinct sets that are coupled through existing boundary conditions. The ease of determining the irrotational, pressure-driven response is offset by the ingenuity required to solve the solenoidal, vorticity-driven response. The latter is relegated to section 5 where the vorticity transport equation is summoned and resolved via regular perturbation tools. Both WKB and multiple-scale procedures are evoked in section 6 to derive simpler formulations, directly from the momentum equation. In section 7, we compare our asymptotics and numerics, and reap, as a windfall, a new similarity parameter that appears in all formulations at any cross-flow Reynolds number. In closing, we retire with final comments in section 8.

2. Model description

2.1. The finite channel

We consider in Fig. 1 the symmetrical influx of a perfect gas into a parallelepiped with two equally permeable walls that are $2h$ apart. We take the channel length L to be larger than the height $2h$ and width w. As shown by Terrill [7], assuming that $w/h \geq 8$ enables us to treat the motion as a case of two-dimensional flow. An orthogonal coordinate system can be anchored at the porous wall with x, y, and z denoting the streamwise, normal, and spanwise coordinates (normalized by h). Due to symmetry about the meridian plane, our investigation can be confined to the range $0 \leq x \leq l$, and $0 \leq y \leq 1$, where $l = L/h$. In additon, we assume that the flow at the downstream end is choked. In Fig. 1, the bulk fluid motion is represented by streamline patterns that denote the undisturbed state. When sinusoidal pressure oscillations are introduced, a more sophisticated temporal field will emerge whose features are yet to be examined.

2.2. Limiting criteria

On the one hand, we limit our scope to low speed injection characterized by a wall Mach number $M = v_w/a_s$ of order 10^{-3}, where a_s is the internal speed of sound. Practically, since a_s far exceeds v_w in most applications, M will be very small. Having identified an ideal candidate for small perturbation expansions, we constrain, on the other hand, the pressure oscillation amplitude A to remain small by comparison to the mean pressure p_s at the channel fore end. This enables us to define another small quantity that scales with A/p_s. Furthermore, in order to maintain consistency in perturbation orders, we limit the channel length to $l < 100$. As we show in the next section, this geometrical restriction is necessary to ensure spatial uniformity in the mean pressure amplitude.

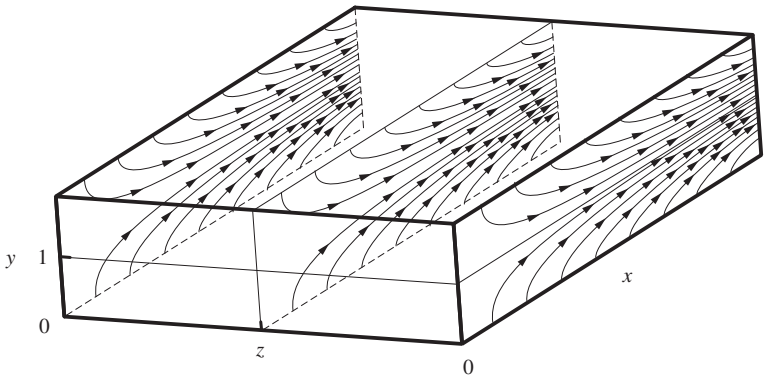

Figure 1.
The planar channel geometry showing typical mean-flow streamlines at three spanwise locations.

2.3. Mean-flow solution

The undisturbed state can be assessed from a classic similarity transformation of the Navier-Stokes equations. As demonstrated by Berman [1], when the steady streamfunction Ψ is chosen to vary linearly in the streamwise direction, one can write, without loss in generality, $\Psi(x, y) = -xF(y)$. Subsequently, the two-dimensional Navier-Stokes equations are reduced into

$$F^{iv} + R(F'F'' - FF''') = 0, \tag{2.1}$$

where, in our notation, $R = v_w h/\nu > 0$ for injection. The corresponding velocity and vorticity vectors, normalized by v_w can be expressed as $\mathbf{u}_0 = u_0\hat{\mathbf{i}} + v_0\hat{\mathbf{j}}$, and $\mathbf{\Omega}_0 = \nabla \times \mathbf{u}_0 = \Omega_0\hat{\mathbf{k}}$,

$$u_0 = -xF',\ v_0 = F, \text{ and } \Omega_0 = xF''. \tag{2.2}$$

These must fulfil the no-slip condition, $u_0(x, 0) = 0$, and the normal influx at the wall, $v_0(x, 0) = 1$. Furthermore, symmetry about the meridian plane demands that $\partial u_0(x, 1)/\partial y = 0$, and $v_0(x, 1) = 0$. The assortment of four boundary conditions on F translates into,

$$F'(0) = F(1) = F''(1) = 0, \text{ and } F(0) = 1. \tag{2.3}$$

As shown in a survey by Terrill [7], various asymptotic solutions are available for different values of R. Despite our aim geared towards a formulation that would be applicable to an arbitrary F, we are inclined to invoke, occasionally, simple solutions that can be used as vehicles for verification and added physical clarity.

To that end, we furnish below two asymptotic formulae by Berman [1] and Yuan [4] that correspond to either small or large wall injection:

$$F(y) = \begin{cases} 1 - \frac{3}{2}y^2 + \frac{1}{2}y^3 + \mathcal{O}(10^{-2}R), \text{ small } R \\ \cos(\frac{\pi}{2}y) + \mathcal{O}(R^{-1}), \text{ large } R \end{cases} \tag{2.4}$$

The mean pressure associated with (2.2) can be normalized by γp_s, where γ is the ratio of specific heats, and then integrated from the ideal momentum equation, $M^2\mathbf{u}_0 \cdot \nabla\mathbf{u}_0 = -\nabla p_0$. Recalling that $a_s = \sqrt{(\gamma p_s/\rho_s)}$, and that the stagnation pressure condition $p_0(0,1) = 1/\gamma$ must be satisfied at the fore end, we gather, after some algebra,

$$p_0(x,y) = 1/\gamma - \frac{1}{2}M^2[F^2 + (F'^2 - FF'')x^2] = 1/\gamma + \mathcal{O}(M^2x^2). \tag{2.5}$$

Equation (2.5) indicates that the error associated with a uniform pressure distribution will be less than a few percent as long as $x \leq 100$. This justifies the upper limit posted earlier on the channel length.

3. Linearized Navier-Stokes equations

3.1. Representation

The differential conservation of mass and momentum principles can be expressed in the familiar dimensionless form

$$\partial\widehat{\rho}/\partial t + \nabla \cdot (\widehat{\rho}\widehat{\mathbf{u}}) = 0, \tag{3.1}$$

$$\widehat{\rho}[\partial\widehat{\mathbf{u}}/\partial t + (\widehat{\mathbf{u}} \cdot \nabla)\widehat{\mathbf{u}}] = -\nabla\widehat{p} + \bar{R}^{-1}[4\nabla(\nabla \cdot \widehat{\mathbf{u}})/3 - \nabla \times (\nabla \times \widehat{\mathbf{u}})]. \tag{3.2}$$

As we employ asterisks to denote dimensional counterparts, the total instantaneous velocity, pressure, density, spatial coordinates and time are normalized in the following fashion:

$$\widehat{\mathbf{u}} = \widehat{\mathbf{u}}^*/a_s,\ \widehat{p} \equiv \widehat{p}^*/(\gamma p_s),\ \widehat{\rho} \equiv \widehat{\rho}^*/\rho_s,\ x = x^*/h,\ y = y^*/h, \text{ and } t = t^*a_s/h. \tag{3.3}$$

Following these transformations, $\bar{R} = a_s h/\nu$ will designate the so-called acoustic Reynolds number.

3.2. Variable decomposition

When small oscillations are introduced at a circular frequency ω, the instantaneous pressure can be represented by a linear sum of its steady and time-dependent fluctuations. Using subscripts for perturbation orders, we follow Lighthill [28] in expanding the total pressure into

$$\widehat{p}^* = p_0^*(x^*, y^*) + p_1^*(x^*, y^*, t^*) = p_0^* + AP(x^*, y^*) \exp(-i\omega t^*), \tag{3.4}$$

where P is a spatial function of $\mathcal{O}(1)$ that will be determined in section 4.4. Normalizing and using $p_0^* = p_s$, one obtains

$$\widehat{p}(x, y, t) = 1/\gamma + \bar{\epsilon} P(x, y) \exp(-ik_m t) \simeq 1/\gamma + \bar{\epsilon} p_1(x, y, t), \tag{3.5}$$

where $\omega_m = \omega h/a_s$ is the nondimensional frequency, and $\bar{\epsilon} = A/(\gamma p_s)$ is the wave amplitude ratio. Density can be expanded in a similar fashion. If ρ_1 is of $\mathcal{O}(1)$, we can set $\rho_1^* \equiv \bar{\epsilon}\rho_s\rho_1$, and write

$$\widehat{\rho} = (\rho_s + \rho_1^*)/\rho_s = 1 + \bar{\epsilon}\rho_1. \tag{3.6}$$

In much the same way, velocity lends itself to decomposition given small velocity oscillations about the mean. At the outset, we write

$$\widehat{\mathbf{u}}^* = \mathbf{u}_0^* + \mathbf{u}_1^* = v_w \mathbf{u}_0 + \mathbf{u}_1^*. \tag{3.7}$$

Setting $\mathbf{u}_1^* \equiv \bar{\epsilon} a_s \mathbf{u}_1$, we normalize by a_s and reap, for the total velocity and vorticity vectors,

$$\widehat{\mathbf{u}} = M\mathbf{u}_0 + \bar{\epsilon}\mathbf{u}_1, \text{ and } \widehat{\boldsymbol{\Omega}} = M\boldsymbol{\Omega}_0 + \bar{\epsilon}\boldsymbol{\Omega}_1. \tag{3.8}$$

3.3. Navier-Stokes linearization

When the perturbed pressure, velocity, and density are inserted back into (3.1)–(3.2), they precipitate two sets of equations depending on the order of the wave amplitude. On the one hand, the zero-order set reduces to Berman's nonlinear equation that is automatically satisfied by the mean flow. On the other hand, the first-order set in the wave amplitude can be segregated to provide the fundamental interaction equations that govern the time-dependent field:

$$\partial\rho_1/\partial t + \nabla \cdot \mathbf{u}_1 = -M\nabla \cdot (\rho_1 \mathbf{u}_0), \tag{3.9}$$

$$\begin{aligned} \partial\mathbf{u}_1/\partial t = &-M\left[\nabla(\mathbf{u}_0 \cdot \mathbf{u}_1) - \mathbf{u}_1 \times \boldsymbol{\Omega}_0 - \mathbf{u}_0 \times \boldsymbol{\Omega}_1\right] \\ &- \nabla p_1 + \bar{R}^{-1}\left[4\nabla(\nabla \cdot \mathbf{u}_1)/3 - \nabla \times \boldsymbol{\Omega}_1\right]. \end{aligned} \tag{3.10}$$

This linear set embodies the influence of mean fluid motion on the oscillatory field.

4. Vector superposition

4.1. Flow field decomposition

The temporal disturbances can be decomposed into separate curl-free and divergence-free components. To that end, the former is taken to be the gradient of a scalar ϕ, and the latter is taken to be the curl of a vector $\mathbf{V}$. When the circumflex and tilde are used to designate irrotational and solenoidal parts, the time-dependent velocity can be partitioned into

$$\mathbf{u}_1 = \hat{\mathbf{u}} + \tilde{\mathbf{u}} \equiv \nabla\phi + \nabla \times \mathbf{V}. \tag{4.1}$$

From (4.1), the conditions $\nabla \times \hat{\mathbf{u}} = 0$ and $\nabla \cdot \tilde{\mathbf{u}} = 0$ are self-evident. Similar decomposition of small disturbances into irrotational, pressure-driven responses and rotational, vorticity-driven responses has been accomplished previously by Chu and Kovsznay [29], Carrier and Carlson [30], and others. From (4.1), it follows that

$$\boldsymbol{\Omega}_1 \equiv \nabla \times \mathbf{u}_1 = \tilde{\boldsymbol{\Omega}} \equiv \nabla \times \tilde{\mathbf{u}}, \ p_1 = \hat{p}, \text{ and } \rho_1 = \hat{\rho}. \tag{4.2}$$

Clearly, unsteady vorticities owe their presence to the rotational response and oscillatory pressures are associated with the irrotational response. The last term in (4.2) stems from the known relation, $\hat{p} = \hat{\rho}$, for a perfect gas undergoing isentropic oscillations.

4.2. Governing responses

When (4.1)–(4.2) are substituted back into (3.9)–(3.10), two distinct sets of formulae are reproduced. The two sets, given below, remain coupled through existing boundary conditions.

4.2.1. Pressure-driven response

$$\partial\hat{\rho}/\partial t + \nabla \cdot \hat{\mathbf{u}} = -M\nabla \cdot (\hat{\rho}\mathbf{u}_0), \tag{4.3}$$

$$\partial\hat{\mathbf{u}}/\partial t = -\nabla\hat{p} - M\left[\nabla(\hat{\mathbf{u}} \cdot \mathbf{u}_0) - \hat{\mathbf{u}} \times \boldsymbol{\Omega}_0\right] + 4\bar{R}^{-1}\nabla(\nabla \cdot \hat{\mathbf{u}})/3. \tag{4.4}$$

4.2.2 Vorticity-driven response

$$\nabla \cdot \tilde{\mathbf{u}} = 0, \tag{4.5}$$

$$\partial\tilde{\mathbf{u}}/\partial t = -M\left[\nabla(\tilde{\mathbf{u}} \cdot \mathbf{u}_0) - \tilde{\mathbf{u}} \times \boldsymbol{\Omega}_0 - \mathbf{u}_0 \times \tilde{\boldsymbol{\Omega}}\right] - \bar{R}^{-1}\nabla \times \tilde{\boldsymbol{\Omega}}. \tag{4.6}$$

4.3. Boundary conditions

On the one hand, the no-slip condition demands that the component of velocity parallel to the wall be zero. This implies that $u_1(x,0) = 0$, or $\hat{u}(x,0) + \tilde{u}(x,0) = 0$, thus providing a strong dynamic coupling between pressure and vortical disturbances at the wall. On the other hand, symmetry along the midsection plane implies that $\partial u_1(x,1)/\partial y = 0$.

4.4. Irrotational solution

Bearing in mind that $\hat{p} = \hat{\rho}$, a standard rearrangement of (4.3)–(4.4) reduces the set into

$$\partial^2 \hat{p}/\partial t^2 - \nabla^2 \hat{p} = -M \left[\nabla \cdot (\mathbf{u}_0 \partial \hat{p}/\partial t) - \nabla^2 (\hat{\mathbf{u}} \cdot \mathbf{u}_0) + \nabla \cdot (\hat{\mathbf{u}} \times \mathbf{\Omega}_0) \right]. \tag{4.7}$$

Equation (4.7) possesses a well-known solution at $\mathcal{O}(M)$. In fact, separation of variables can be used in unison with the rigid wall boundary conditions to reproduce the solution corresponding to longitudinal oscillations in a channel with $l \gg 1$. When expressed in Euler's notation, the oscillatory pressure reads

$$\hat{p}(x,t) = \cos(\omega_m x) \exp(-i\omega_m t) + \mathcal{O}(M). \tag{4.8}$$

Here $\omega_m = \omega h/a_s = m\pi/l$ is the dimensionless wave number and $m = 1, 2, 3, \ldots$ denotes the oscillation mode number. The corresponding velocity response can be integrated from (4.4) to obtain

$$\hat{\mathbf{u}}(x,t) = i \sin(\omega_m x) \exp(-i\omega_m t) \hat{\mathbf{i}} + \mathcal{O}(M). \tag{4.9}$$

4.5. Rotational equations

The oscillatory vortical response can be expressed as

$$\tilde{\mathbf{u}}(x,y,t) = \bar{\mathbf{u}}(x,y) \exp(-i\omega_m t), \;\; \tilde{\mathbf{\Omega}}(x,y,t) = \bar{\mathbf{\Omega}}(x,y) \exp(-i\omega_m t). \tag{4.10}$$

where $\bar{\mathbf{u}} \equiv \bar{u}\hat{\mathbf{i}} + \bar{v}\hat{\mathbf{j}}$, and $\bar{\mathbf{\Omega}} \equiv \nabla \times \bar{\mathbf{u}} = \bar{\Omega}\hat{\mathbf{k}}$. In lieu of (4,5) and (4.6), we now have

$$\nabla \cdot \bar{\mathbf{u}} = 0, \tag{4.11}$$

$$i\bar{\mathbf{u}} = \left[\nabla(\bar{\mathbf{u}} \cdot \mathbf{u}_0) - \bar{\mathbf{u}} \times \mathbf{\Omega}_0 - \mathbf{u}_0 \times \bar{\mathbf{\Omega}} \right] / S + \nabla \times \bar{\mathbf{\Omega}}/K, \tag{4.12}$$

where

$$S = \frac{\omega_m}{M} = \frac{\omega h}{v_w}, \text{ and } K = \omega_m \bar{R} = \frac{\omega h^2}{\nu} = \frac{h^2}{\left(\sqrt{\nu/\omega}\right)^2}. \tag{4.13}$$

The dynamic similarity parameters in (4.12) are the Strouhal number S, and the kinetic Reynolds number K. The latter is the quotient of the global length scale h to the much smaller Stokes layer thickness $\sqrt{(\nu/\omega)}$ raised to the second power. Since $\sqrt{(\nu/\omega)} \ll h$, we define $\epsilon \equiv 1/K$ to be our primary perturbation parameter. This parameter belongs to the practical range $10^{-8} < \epsilon < 10^{-4}$. Furthermore, since oscillatory flows are characterized by appreciable Strouhal numbers, we define $\sigma = 1/S < 0.1$. Note that ϵ is always smaller than σ by virtue of their ratio $\sigma/\epsilon = v_w h/\nu = R > 1$, irrespective of frequency.

Based on foreknowledge and numerical verifications, we now make the conditional stipulation that $\bar{v}/\bar{u}$ must be of $\mathcal{O}(M)$. Subject to dual confirmations at the conclusion of the forthcoming analysis, this proviso is necessary at this point to overcome technical obstructions arising in the governing equations. Since our final solution is limited by the $\mathcal{O}(M)$ error associated with the pressure response, $\bar{v}$ can be omitted at the first perturbation level. On that account, the axial component of (4.12) reduces to

$$\begin{aligned} i\bar{u} &= \sigma\left[\frac{\partial}{\partial x}(\bar{u}u_0) + v_0\frac{\partial \bar{u}}{\partial y}\right] - \epsilon\frac{\partial^2 \bar{u}}{\partial y^2} + \mathcal{O}(M), \text{ or} \\ i\bar{u} &= \sigma\left[\frac{\partial}{\partial x}(\bar{u}u_0) - v_0\bar{\Omega}\right] + \epsilon\frac{\partial \bar{\Omega}}{\partial y} + \mathcal{O}(M). \end{aligned} \tag{4.14}$$

5. Vorticity transport formulation

5.1. Governing equation

The vorticity transport equation can be obtained by performing the curl on (4.12). Moreover, when Euler's notation is used, one gets, at $\mathcal{O}(M)$,

$$i\bar{\mathbf{\Omega}} = -\sigma\nabla \times (\bar{\mathbf{u}} \times \mathbf{\Omega}_0 + \mathbf{u}_0 \times \bar{\mathbf{\Omega}}) - \epsilon\nabla^2\bar{\mathbf{\Omega}}. \tag{5.1}$$

In scalar form, this can be rearranged in a manner to place leading-order quantities on the left-hand side:

$$\frac{\partial \bar{\Omega}}{\partial y} - \frac{i\bar{\Omega}}{\sigma v_0} + \frac{u_0}{v_0}\frac{\partial \bar{\Omega}}{\partial x} = -\frac{\bar{u}}{v_0}\frac{\partial \Omega_0}{\partial x} + \frac{\epsilon}{\sigma v_0}\left(\frac{\partial^2 \bar{\Omega}}{\partial x^2} + \frac{\partial^2 \bar{\Omega}}{\partial y^2}\right) \tag{5.2}$$

In (5.2), the right-hand side quantities represent the axial convection of mean-flow vorticity by virtue of the oscillatory vortical action, and the viscous diffusion of unsteady vorticity. Both are secondary effects that can be ignored at the zero perturbation level. Vorticity can be expanded in powers of M, via $\bar{\Omega} = \bar{\omega}_0 + M\bar{\omega}_1 + \mathcal{O}(M^2)$, and later substituted into (5.2). The leading-order equation that follows, namely,

$$\frac{\partial \bar{\omega}_0}{\partial y} - \frac{i\bar{\omega}_0}{\sigma v_0} + \frac{u_0}{v_0}\frac{\partial \bar{\omega}_0}{\partial x} = 0, \tag{5.3}$$

suggests investigating a separable solution of the type $\bar{\omega}_0 = X(x)Y(y)$. When this form is inserted into (5.3), we reap

$$\bar{\omega}_0(x,y) = \sum_{\lambda_n} c_n (xF)^{\lambda_n} \exp(-i\Phi_0), \tag{5.4}$$

where the phase lead of the vortical wave is dependent on

$$\Phi_0(y) = -S\int_0^y \frac{dz}{F(z)} = \begin{cases} -\dfrac{1}{3}S\left[\ln(1+y-\dfrac{1}{2}y^2) - \ln(1-y)^2\right], \text{ small } R \\ -\dfrac{2}{\pi}S\ln\tan\left[\dfrac{\pi}{4}(1+y)\right] = -\dfrac{2}{\pi}S\mathrm{gd}^{-1}(\dfrac{\pi}{2}y), \text{ large } R \end{cases} \tag{5.5}$$

For the large injection case, $\mathrm{gd}(z) = 2\arctan(z) - \frac{\pi}{2}$ is the Gudermannian function described in Abramowitz and Stegun [31]. Note that $\bar{\omega}_0$ contains a denumerable set of arbitrary constants c_n that must be specified in a manner to satisfy the no-slip condition at the wall, written for vorticity. This requires a careful treatment and is examined next.

5.2. Pressure-driven vorticity at the wall

Recalling that $\Omega_1 = \tilde{\Omega}$, $v_1 = \tilde{v}$, $p_1 = \hat{p}$, and that $u_1(x,0,t)$ must vanish to prevent slippage, the axial projection of (3.10) reduces, at the wall, into

$$0 = -M\left[\frac{\partial}{\partial x}(\tilde{v}v_0) - \tilde{v}\Omega_0 - v_0\tilde{\Omega}\right] - \frac{\partial \hat{p}}{\partial x} - \frac{1}{R}\frac{\partial \tilde{\Omega}}{\partial y}. \tag{5.6}$$

Rearranging, and using the fact that $\hat{p} = \cos(\omega_m x)\exp(-i\omega_m t)$, the no-slip condition translates into

$$\begin{aligned} \tilde{\Omega} &= \frac{1}{M}\frac{\partial \hat{p}}{\partial x} + \frac{\epsilon}{\sigma}\frac{\partial \tilde{\Omega}}{\partial y} + \frac{\partial \tilde{v}}{\partial x} - x\tilde{v}F''(0) \\ &= -S\sin(\omega_m x)\exp(-i\omega_m x) + \frac{\epsilon}{\sigma}\frac{\partial \tilde{\Omega}}{\partial y} + \mathcal{O}(M), \end{aligned} \tag{5.7}$$

which can be recast into

$$\bar{\Omega}(x,0) = -S\sin(\omega_m x) + \frac{1}{R}\frac{\partial \bar{\Omega}}{\partial y} + \mathcal{O}(M). \tag{5.8}$$

It can be realized from (5.8) that vorticity originates at the wall where the oscillatory pressure gradient is perpendicular to incoming fluxes. Furthermore, vorticity generation is highest at pressure nodes located at $x/l = (2m-1)/(2m)$, where the inviscid, pressure-driven $\hat{u}$ has maximum amplitude.

5.3. Inviscid vorticity

At the wall, (5.8) must be equated to (5.4) in order to specify the separation eigenvalues. Thus, since $F(0) = 1$, and $\Phi_0(0) = 0$, then

$$\bar{\omega}_0(x,0) = \sum_{\lambda_n} c_n x^{\lambda_n} = -S\sin(\omega_m x) \equiv -S\sum_{n=0}^{\infty} \frac{(-1)^n(\omega_m x)^{2n+1}}{(2n+1)!}, \tag{5.9}$$

whence

$$\bar{\omega}_0(x,y) = S\left[\sum_{n=0}^{\infty} \frac{(-1)^n}{(2n+1)!}(-\omega_m x F)^{2n+1}\right]\exp(-i\Phi_0). \tag{5.10}$$

From section 2.3, we recall that $\Psi = -xF$, and thus identify the infinite series between braces to be a sine function of Ψ. At the outset, we let $Z_m(x,y) \equiv \omega_m\Psi(x,y)$, and simplify (5.10) into

$$\bar{\omega}_0(x,y) = S\sin(Z_m)\exp(-i\Phi_0). \tag{5.11}$$

5.4. Inviscid streamfunction

At this juncture, one can resort to the oscillatory streamfunction to replace the velocity components via $\bar{u} = \partial\psi/\partial y$ and $\bar{v} = -\partial\psi/\partial x$. At the outset, the vorticity equation becomes,

$$\bar{\Omega} = -\frac{\partial^2\psi}{\partial x^2} - \frac{\partial^2\psi}{\partial y^2}. \tag{5.12}$$

We then proceed heuristically by suggesting the ansatz $\psi_0(x,y) = \psi_c(y)\bar{\omega}_0(x,y)$. This is based on the assumption that ψ must possess the same axial dependence as $\bar{\Omega}$. When inserted back into (5.12), a balance between leading-order quantities of comparable size yields

$$\psi_c = \sigma^2F^2 \Rightarrow \psi_0 = \sigma F^2\sin(Z_m)\exp(-i\Phi_0). \tag{5.13}$$

Subsequently, the inviscid, vortical component of the oscillatory velocity can be deduced by simple differentiation. The result is

$$\bar{\mathbf{u}}(x,y) = \left[iF\sin(Z_m)\hat{\mathbf{i}} + MF^3\cos(Z_m)\hat{\mathbf{j}}\right]\exp(-i\Phi_0). \tag{5.14}$$

5.5. Viscous corrections

Following the same perturbative scheme, we set an ansatz for each of the velocity and vorticity terms. Assuming that both $\bar{u}$ and $\bar{\Omega}$ must possess the same axial dependence as their inviscid counterparts, we set

$$\begin{aligned} \bar{u}(x,y) &= u_c(y)\sin(Z_m)\exp(-i\Phi_0), \text{ and} \\ \bar{\Omega}(x,y) &= \bar{\omega}_c(y)\sin(Z_m)\exp(-i\Phi_0). \end{aligned} \tag{5.15}$$

The viscous correction multipliers, u_c and $\bar{\omega}_c$, must be found in a manner to satisfy the complete vorticity transport equation. In fact, when we substitute (5.15) into (5.2), we note the cancellation of several terms. Balancing the remaining leading-order quantities demands that

$$d\bar{\omega}_c/dy + \epsilon S^3 F^{-3}\bar{\omega}_c + F'' F^{-1} u_c + \mathcal{O}(M,\sigma^2) = 0, \tag{5.16}$$

where $\xi = \epsilon S^3 = \omega^2 \nu h v_w^{-3}$ appears as a dynamic similarity parameter. At this point, a relationship between u_c and $\bar{\omega}_c$ is needed to make any headway. On that account, we resort to (4.14) and find

$$u_c = \sigma(iF + \xi\sigma F^{-1})\bar{\omega}_c + \mathcal{O}(M,\sigma^2). \tag{5.17}$$

Inserting this formula into (5.16) leads to:

$$d\bar{\omega}_c/dy + (\xi F^{-3} + i\sigma F'')\bar{\omega}_c + \mathcal{O}(M,\sigma^2) = 0, \tag{5.18}$$

which, after some algebra, gives

$$\bar{\omega}_c(y) = C\exp\zeta, \tag{5.19}$$

It may be instructive to note that, for consistency in perturbation orders, one must suppress the imaginary argument in ζ which is of effective $\mathcal{O}(\sigma^2)$. The reason is that this spurious argument that appears at $\mathcal{O}(\sigma)$ must be added eventually to the leading-order $\Phi_0 \sim \sigma^{-1}$. The damping function ζ can thus be evaluated from

$$\frac{\zeta}{\xi} = -\int_0^y F^{-3}(z)dz = \begin{cases} -\dfrac{4}{27}\ln\dfrac{3-\bar{y}^2}{2\bar{y}^2} - \dfrac{4\bar{y}^4 - 18\bar{y}^2 + 12}{9\bar{y}^2(3-\bar{y}^2)^2} - \dfrac{1}{18}, & \text{small } R \\ -\dfrac{1}{\pi}\left[\ln\tan\dfrac{\pi}{4}(1+y) + \sec(\dfrac{\pi}{2}y)\tan(\dfrac{\pi}{2}y)\right], & \text{large } R \end{cases}, \tag{5.20}$$

$$\bar{y} = 1 - y.$$

5.6. Vorticity correction

The integration constant C can be specified from (5.8). In fact, when (5.19) is implemented to update the vorticity boundary condition at the wall, we observe, at $\mathcal{O}(M, \sigma^2)$ that

$$C\left\{1-\xi\sigma^2\left[\zeta'(0)-i\Phi_0(0)\right]\right\}\sin[Z_m(x,0)]\exp[\zeta(0)-i\Phi_0(0)] = -S\sin(\omega_m x), \tag{5.21}$$

where

$$\begin{gathered}\zeta'(0) = -\xi F^{-3}(0) = -\xi;\ \Phi_0'(0) = -SF^{-1}(0) = -S;\\ \text{and } \zeta(0) = \Phi_0(0) = 0,\ \forall F.\end{gathered} \tag{5.22}$$

Direct substitution into (5.21) gives $C(1-i\xi\sigma) = S+\mathcal{O}(\sigma^2)$. When the superscripts 'r' and 'i' are used to denote real and imaginary parts, the constant C can be expressed by

$$C^r = \frac{S^3}{S^2+\xi^2},\ C^i = \frac{\xi S^2}{S^2+\xi^2}. \tag{5.23}$$

Straightforward substitution into (5.19), (5.15), and (4.10) yields, at last,

$$\tilde{\Omega}(x,y,t) = C\sin(Z_m)\exp(\zeta - i\Phi_0 - i\omega_m t). \tag{5.24}$$

5.7. Axial velocity correction

In much the same way, the corrective multiplier u_c can be deduced from (5.17), viz.

$$u_c = \sigma(iF+\xi\sigma F^{-1})C\exp\zeta \equiv iU\exp\zeta, \tag{5.25}$$

where

$$U^r = \sigma(C^rF+\xi\sigma C^i/F),\ U^i = \sigma(C^iF-\xi\sigma C^r/F), \tag{5.26}$$

so that $\tilde{\mathbf{u}}$ is soluble by backward substitution into (5.15) and (4.10). At length, we find that

$$\tilde{u}(x,y,t) = \bar{u}\exp(-i\omega_m t) = iU\sin(Z_m)\exp(\zeta - i\Phi_0 - i\omega_m t). \tag{5.27}$$

5.8. Normal velocity correction

The normal component $\tilde{v}$ can be elicited in a manner to satisfy mass conservation. In practice, this process is expedited by assuming that

$$\tilde{v} = g(y)\cos(Z_m)\exp(\zeta - i\Phi_0 - i\omega_m t). \tag{5.28}$$

Direct substitution into (4.5) produces $g(y)$. In fact, satisfaction of $\partial\tilde{v}/\partial y + \partial\tilde{u}/\partial x = 0$ demands that $g = MUF^2$. Therefore,

$$\tilde{v}(x,y,t) = MUF^2\cos(Z_m)\exp(\zeta - i\Phi_0 - i\omega_m t), \tag{5.29}$$

which lends support to the earlier stipulation, in section 4.5, contending that $\tilde{v}/\tilde{u} = \mathcal{O}(M)$.

5.9. The total time-dependent solution

For the reader's convenience, we retrace our steps and summarize the results of the current procedure. The real components of time-dependent velocity and vorticity are hence revisited below. Using the superscript 'V' to refer to the vorticity transport formulation, we list

$$\begin{gathered} u_1^V = \sin(\omega_m x)\sin(\omega_m t) - (U^r\sin\varphi - U^i\cos\varphi)\exp\zeta\sin(\omega_m xF), \\ \varphi = \omega_m t + \Phi_0 \end{gathered} \tag{5.30}$$

$$v_1^V = -MF^2(U^r\cos\varphi + U^i\sin\varphi)\exp\zeta\cos(\omega_m xF), \tag{5.31}$$

$$\Omega_1^V = -(C^r\cos\varphi + C^i\sin\varphi)\exp\zeta\sin(\omega_m xF). \tag{5.32}$$

Note that the first term in (5.30) may be envisaged as the inviscid, irrotational response to the oscillatory pressure while the second may be held accountable for the viscous, vortical response due to the presence of solid boundaries. Naturally, the second response decays asymptotically with increasing distance from the wall.

6. Momentum transport formulation

6.1. Governing equation

In the previous section, the rotational velocity was obtained from the vorticity and vorticity transport equations following a number of successive approximations. At present, $\tilde{u}$ will be derived directly from the momentum equation, written at $\mathcal{O}(M)$. To that end, we first rearrange (4.14) into

$$x\frac{\partial\bar{u}}{\partial x} = -\frac{S}{F'}\left[(i+\sigma F')\bar{u} - \sigma F\frac{\partial\bar{u}}{\partial y} + \epsilon\frac{\partial^2\bar{u}}{\partial y^2}\right] + \mathcal{O}(M), \tag{6.1}$$

and then call for separation of variables in order to investigate a solution of the form $\bar{u}(x,y) = X(x)Y(y)$. Substitution into (6.1) renders,

$$\frac{x}{X}\frac{dX}{dx} = -\frac{S}{F'Y}\left[\epsilon\frac{d^2Y}{dy^2} - \sigma F\frac{dY}{dy} + (i+\sigma F')Y\right] = \lambda_n, \tag{6.2}$$

where λ_n must be positive for a nontrivial solution. Integration of the x-equation is straightforward. The result is $X_n(x) = c_n x^{\lambda_n}$, where c_n is an integration constant tied to λ_n. Owing to the linearity of (6.1), the general solution becomes

$$\bar{u}(x,y) = \sum_{\lambda_n} c_n x^{\lambda_n} Y_n(y) \tag{6.3}$$

where λ_n must be determined from the no-slip boundary condition at the wall written for the velocity. As specified in section 4.3, this condition is fulfilled when, $\bar{u}(x,0) = -i\sin(\omega_m x)$. Writing out the MacLaurin series expansion for the sine function, and equating the result to (6.3) gives,

$$\sum_{\lambda_n} c_n x^{\lambda_n} Y_n(0) \equiv -i\sum_{n=0}^{\infty}\frac{(-1)^n(\omega_m x)^{2n+1}}{(2n+1)!}, \tag{6.4}$$

which precipitates,

$$\lambda_n = 2n+1,\ n=0,1,2,\ldots,\ c_n = -i\frac{(-1)^n(\omega_m x)^{2n+1}}{(2n+1)!},\ Y_n(0)=1, \tag{6.5}$$

wherefore,

$$\bar{u}(x,y) = -i\sum_{n=0}^{\infty}\frac{(-1)^n(\omega_m x)^{2n+1}}{(2n+1)!}Y_n(y). \tag{6.6}$$

The velocity eigenfunction Y_n is left to be determined from (6.2) via

$$\epsilon\frac{d^2Y_n}{dy^2} - \sigma F\frac{dY_n}{dy} + [i+2\sigma(n+1)F']Y_n = 0,\ 0\le y\le 1, \tag{6.7}$$

with boundary conditions,

$$Y_n(0) = 1 \text{ (no-slip at the wall), and } Y_n'(1) = 0 \text{ (core symmetry).} \tag{6.8}$$

By virtue of (2.3), (6.7) admits a regular singularity at the core where $F(1) = 0$. Evidently, the presence of a small multiplier in the highest derivative evokes the possibility of a perturbation treatment. In fact, both WKB and two-variable multiple-scale expansions appear promising. For example, the two-variable derivative expansion technique was shown in a previous work [32] to result in locally valid

solutions corresponding to inner, outer, and transition scales. As described therein, a uniform two-scale expansion could also be attained using a hybrid technique. The latter was based on the choice of a composite scale that could reproduce the inner, outer, and transition scales in their respective domains.

In the current investigation, we shall use a different strategy. Instead of constructing the so-called composite scale from our foreknowledge of inner, outer, and transition scales, we shall leave the modified variable unspecified while carrying out the two-scale expansion. At the conclusion of the asymptotic analysis, physical arguments will be employed to solve for the undetermined coordinate transformation. Before initiating the asymptotic work, we define u_1^N to be the numerical solution of the linearized momentum equation, given by (4.14). In fact, u_1^N can be determined by coupling the numerical solution to (6.7), specified in [32], with (6.6), (4.10), (4.1), and (4.9).

6.2. The WKB approach

While seeking an asymptotic solution for (6.7), two cases must be considered separately depending on the order of the secondary perturbation parameter σ. Our motivation is this:

6.2.1. The traditional outer expansion. For $\sigma = \mathcal{O}(1)$, the leading-order term of the outer solution Y_n^o can be resolved via

$$-\sigma F Y_n^{o\prime} + [i + \sigma(2n+2)F']\, Y_n^o = 0,\ Y_n^o(0) = 1,$$
$$\Rightarrow\ Y_n^o(y) = F^{2n+2} \exp\left[iS \int_0^y F^{-1}(z)dz\right], \quad (6.9)$$

with

$$\Re[Y_n^o(y)] = F^{2n+2} \cos\left[S \int_0^y F^{-1}(z)dz\right]. \quad (6.10)$$

Recalling from (2.3) that all solutions to Berman's equation must satisfy $F(1) = 0$, we realize that the F^{2n+2} factor in the outer solution decays rapidly as $y \to 1$. Clearly, the decay is more rapid at higher eigenvalues. As a result, the remaining boundary condition at the origin is automatically satisfied by the first derivative. This obviates the need for an inner solution at this order. As made obvious in (6.10), the exponential term in Y_n^o represents an oscillatory behaviour that is rapid for large S. Since S could be large in real applications, the rapid oscillations that occur on a shorter length scale preclude the possibility of a uniformly valid solution. This becomes apparent in the first-order correction when Y_n^o is written at $\mathcal{O}(\epsilon^2)$:

$$Y_n^o = F^{2n+2} \exp(-i\Phi)\Big(1 + \epsilon S \int_0^y \{-S^2 + 2(n+1)[FF''$$
$$+ (2n+1)F'^2] + i(4n+3)SF'\}F^{-3}dz\Big). \quad (6.11)$$

Realizing that the correction term contains a part of $\mathcal{O}(\epsilon S^3)$, nonuniformity is expected when S becomes large. At this point, a WKB strategy becomes more suitable.

6.2.2. The WKB ansatz. For small σ, rapid oscillations occur on a short length scale, and a slow drift takes place on the scale $x = \mathcal{O}(1)$. The leading-order equation that delivers the WKB ansatz is

$$-FY_n' + iSY_n = 0,\ Y_n(0) = 1, \Rightarrow Y_n(y) = \exp\left[iS\int_0^y F^{-1}(z)dz\right]. \tag{6.12}$$

Equation (6.12) evokes setting $Y_n(y) = g(y)\exp(-i\Phi_0)$ and revisiting (6.7). At the outset, we segregate terms of $\mathcal{O}(\epsilon S^2)$ and harvest

$$\begin{aligned} g' + \left[\epsilon S^3 F^{-3} - 2(n+1)F^{-1}F'\right] g &= i\epsilon S^2 F^{-2}(2g' - F^{-1}F'g) + \epsilon S F^{-1} g'' \\ &= \mathcal{O}(\epsilon S^2). \end{aligned} \tag{6.13}$$

The WKB solution can be extracted therefrom, namely,

$$Y_n^W(y) = F^{2n+2}\exp(\zeta_0 - i\Phi_0) + \mathcal{O}(\epsilon S^2),\ \zeta_0 = -\xi\int_0^y F^{-3}(z)dz; \tag{6.14}$$

where the superscript 'W' refers to the WKB formulation. The dimensionless group $\xi = \epsilon S^3$ appears to be in control of the exponential rate of decay as $y \to 1$. Note that $Y_n^W(y)$ is uniformly valid and its derivative satisfies the boundary condition at the core.

6.2.3. The WKB solution. Equation (6.14) can be inserted back into (6.6) to give

$$\begin{aligned} \bar{u}(x,y) &= -iF\exp(\zeta_0 - i\Phi_0)\sum_{n=0}^{\infty}\frac{(-1)^n(\omega_m x F)^{2n+1}}{(2n+1)!} \\ &= -iF\exp(\zeta_0 - i\Phi_0)\sin(\omega_m x F). \end{aligned} \tag{6.15}$$

This formula can be used in conjunction with (4.10), (4.9), and (4.1) to construct the total oscillatory velocity component,

$$u_1(x,y,t) = i\sin(\omega_m x)\exp(-i\omega_m t) - iF\exp(\zeta_0 - i\Phi_0 - i\omega_m t)\sin(\omega_m x F). \tag{6.16}$$

Thus, in the real domain, the WKB solution offers

$$u_1^W(x,y,t) = \sin(\omega_m x)\sin(\omega_m t) - F\sin(\omega_m x F)\exp\zeta_0\sin(\omega_m t + \Phi_0). \tag{6.17}$$

6.3. The multiple-scale approach

A two-variable multiple-scale procedure requires specifying two virtual coordinates, an outer scale y_0, and an inner scale, y_1, that enables us to resolve rapidly changing phenomena.

6.3.1 Nonlinear coordinate transformation. Conventional inner scale choices include linear transformations that bear $y_1 = \delta(\epsilon)y$, where $\delta(\epsilon)$ is usually conjectured from foreknowledge, trial-and-error, or a scaling analysis. In the problem at hand, such transformations fail to provide uniformly valid, two-scale expansions. On the contrary, we find it rather useful to introduce a nonlinear variable transformation of the form, $y_1 = \epsilon s(y)$, where $s(y)$ is a general function that can accommodate nonlinear scaling assortments. We find this choice to provide the necessary freedom needed to achieve a balance in the governing equation between diffusive, convective, and inertial terms.

6.3.2. The generalized two-scale expansion Following the procedure described by Majdalani [32], we introduce two virtual coordinates, $y_0 = y$, and $y_1 = \epsilon s(y)$. The difference here is that s will remain unspecified until the conclusion of the asymptotic analysis. Owing to this virtual transformation, functions and derivatives may be expanded in a manner to discard $\mathcal{O}(\epsilon^2)$ and smaller quantities:

$$\begin{aligned} Y_n(y_0, y_1) &= Y^{(0)}(y_0, y_1) + \epsilon Y^{(1)}(y_0, y_1) + \mathcal{O}(\epsilon^2), \\ \frac{d}{dy} &= \frac{\partial}{\partial y_0} + \epsilon \frac{ds}{dy_0}\frac{\partial}{\partial y_1}, \ \frac{d^2}{dy^2} = \frac{\partial^2}{\partial y_0^2} + \mathcal{O}(\epsilon). \end{aligned} \tag{6.18}$$

After inserting these expansions into (6.7), terms of the same order in ε can be segregated to decouple the original equation into

$$\frac{\partial Y^{(0)}}{\partial y_0} - \left[2(n+1)\frac{F'}{F} + i\frac{S}{F}\right] Y^{(0)} = 0, \tag{6.19}$$

$$\frac{\partial Y^{(1)}}{\partial y_0} - \left[2(n+1)\frac{F'}{F} + i\frac{S}{F}\right] Y^{(1)} = -\frac{ds}{dy_0}\frac{\partial Y^{(0)}}{\partial y_1} + \frac{S}{F}\frac{\partial^2 Y^{(0)}}{\partial y_0^2}. \tag{6.20}$$

Boundary conditions given by (6.8) translate into

$$Y^{(0)}(0) = 1, \ \frac{\partial Y^{(0)}}{\partial y_0}(1) = 0. \tag{6.21}$$

Integration of the zero-order equation yields

$$Y^{(0)}(y_0, y_1) = a_1(y_1) \exp\left[2(2n+1)\ln F(y_0) + iS\int_0^{y_0} F^{-1}(z)dz\right] \equiv a_1(y_1)\chi(y_0), \tag{6.22}$$

In preventing the asymptotic series from containing terms whose quotient between two successive orders can be unbounded, the right-hand side of (6.20) must vanish:

$$\Big(- s' \frac{ds_1}{dy_1} + F^{-3} \Big\{ - S^3 + 2S(n+1)[FF'' + (2n+1)F'^2] + iS^2(4n+3)F' \Big\} a_1 \Big) \chi = 0. \quad (6.23)$$

The resulting first-order differential equation in a_1 can be integrated in closed form. Expressed in the original laboratory coordinate, we write

$$a_1(y) = a_0 \exp\left(\xi \eta F^{-3} \{ -1 + 2\sigma^2 (n+1)[F''F + (2n+1)F'^2] + i\sigma(4n+3)F' \} \right). \quad (6.24)$$

where a_0 is a pure constant of integration that must be specified from the boundary condition at the wall. The effective scale functional $\eta(y)$ that appears in (6.24) is the ratio of the scale function and its first derivative, namely,

$$\eta(y) \equiv s(y)/s'(y). \quad (6.25)$$

The rest is straightforward substitution into (6.22). Recalling that the overall solution is sought at $\mathcal{O}(M)$, there is no justification for retaining other than $Y^{(0)}$, and (6.18) reduces, at $\mathcal{O}(\epsilon)$, into

$$Y_n = a_0 F^{2n+2} \exp\left\{ \xi \eta F^{-3} \left[-1 + \sigma^2 (\lambda_n + 1)(F''F + \lambda_n F'^2) \right] + iS \left[\int_0^y F^{-1} dz + \xi \sigma^2 (4n+3) \eta F^{-3} F' \right] \right\}. \quad (6.26)$$

6.3.3. Specifying the undetermined scale Note that both real and imaginary arguments in the exponential above display leading-order quantities followed by smaller terms of $\mathcal{O}(\sigma^2)$. Suppressing these secondary corrections reduces (6.26) to a form that bears a striking resemblance to the WKB solution given by (6.14). In fact, the leading-order terms will be identical to those in Y_n^W when

$$\eta(y) = F^3(y) \int_0^y F^{-3}(z) dz. \quad (6.27)$$

From $\eta(0) = 0$ and $Y_n(0) = 1$ we conclude that $s(0) = 0$ and $a_0 = 1$. As a result, (6.26) will satisfy both boundary conditions stated in (6.21). Having uncovered the effective scale functional in general form, the corresponding undetermined scale can be specified from (6.25). The result is

$$s(y) = \exp \int_0^y \eta^{-1}(z) dz = \exp \int_0^y \frac{F^{-3}(z) dz}{\int_0^z F^{-3}(\tau) d\tau}. \quad (6.28)$$

It may be safe to say that the dependence of the scaling transformation on the Berman function is by no means intuitive. This may explain the difficulty in guessing beforehand the modified coordinate transformation that leads to uniform two-scale expansions. Moreover, we are no longer surprised that the traditional linear transformations of the form $y_1 = \delta(\epsilon)y$ could not prevail.

6.3.4. Comparison for the large injection case For the sake of argument, we consider the large injection case corresponding to $F = \cos(\frac{\pi}{2}y)$. Despite the complexity of equations (6.27) and (6.28), we are able to manage exact expressions for η and s. In fact, after some algebra, we find that

$$\eta(y) = \frac{1}{\pi}\left[\cos(\frac{\pi}{2}y)\ln\tan\frac{\pi}{4}(1+y) + \tan(\frac{\pi}{2}y)\right]\cos^2(\frac{\pi}{2}y), \tag{6.29}$$

$$s(y) = \sec(\frac{\pi}{2}y)\tan(\frac{\pi}{2}y) + \ln\tan\frac{\pi}{4}(1+y). \tag{6.30}$$

Obviously, formula (6.30) precludes the possibility of conjecturing this appropriate coordinate transformation in advance, as required by standard procedures. The most striking result is, perhaps, the agreement between our current didactic formulation and the hybrid formulation obtained by Majdalani [32]. In the previous work, a composite scale $s(y) = y\bar{y}^{-1.5y^{1.5}}$ was initially constructed in a manner to reproduce asymptotically the apparent inner, outer, and transition scales. Usage of the composite scale thus reduced the number of spatial scales to two. This space-reductive step was necessary for the success of the multiple-scale procedure. After devising the composite scale, the effective scale functional $\eta(y) = y/[1 + 1.5y^{1.5}(y\bar{y}^{-1} - 1.5\ln\bar{y})]$ was derived and then inserted into the solution. In the current analysis, the process is somewhat reversed. Here η has to be determined first. Only then could the space-reductive scaling transformation be determined. It may be instructive to note that the nonlinear scaling transformation obtained here is also capable of reproducing near $y = 0, 1$ the local scales proposed in [32].

To gain further reassurance, (6.29) and (6.30) are compared in Fig. 2 with the values of η and s obtained previously using the composite scale technique [32]. It is interesting to note the qualitative agreement which has led, undoubtedly, to two uniformly valid formulations. Furthermore, formula (6.26) can be readily applied to the large injection case. The result will be

$$Y_n = (\cos\theta)^{2n+2}\exp\left\{\xi\eta\sec^3\theta\left[-1 + \frac{\pi^2}{2}\sigma^2(n+1)(2n\sin^2\theta - \cos 2\theta)\right]\right.$$
$$\left. + iS\left[\frac{2}{\pi}\mathrm{gd}^{-1}\theta - \pi\xi\sigma^2(2n+\frac{3}{2})\eta\sec^2\theta\tan\theta\right]\right\} + \mathcal{O}(\epsilon). \tag{6.31}$$

A standard error analysis can be performed on (6.31) to verify the agreement with its counterpart, given by equation (5.22) of the former article [32]. Since the current approach follows precisely the steps outlined in [32], they are omitted

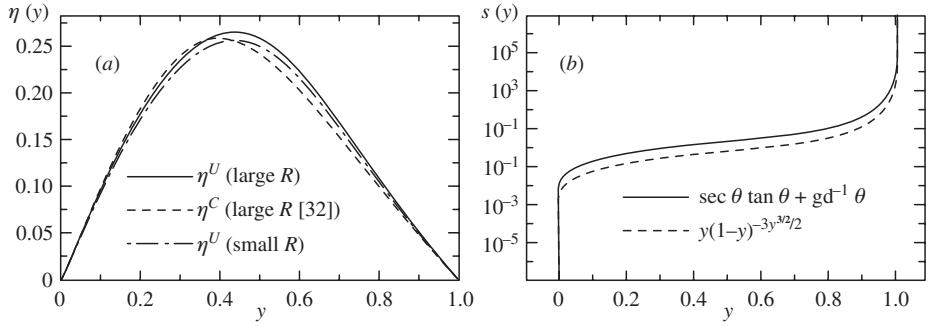

Figure 2.
For the large injection case, we compare in (a) and (b) the currently derived effective scale functional η and its corresponding scaling transformation s to existing composite scale results [32]. Indices 'U' and 'C' refer to the two-variable scheme based on either 'undetermined' or 'composite' scales. For small injection, η is shown in (a) as well.

here. As found previously, results show at $n = 0$ an error of $\mathcal{O}(\epsilon)$ that depreciates incrementally with $n \geq 1$.

A similar analysis can be applied to small injection with $F = 1 - \frac{3}{2}y^2 + \frac{1}{2}y^3$. In fact, for the small R case, results are omitted because they involve long expressions that can be easily reproduced using a symbolic program. For illustration, the corresponding η is included in Fig. 2a.

6.3.5. The multiple-scale solution Having determined Y_n, formula (6.26) can be substituted back into (6.6) and (4.10), and then added to (4.9) via (4.1). At length, we obtain,

$$u_1(x,y,t) = -iF\sum_{n=0}^{\infty}\frac{(-1)^n(\omega_m x F)^{2n+1}}{(2n+1)!}$$
$$\exp\Big(-\xi\eta F^{-3}\{1-2\sigma^2(n+1)[F''F+(2n+1)F'^2]\}$$
$$+iS\left[\int_0^y F^{-1}(\zeta)d\zeta+\sigma^2\xi\eta F^{-3}(4n+3)F'\right]$$
$$-i\omega_m t\Big)+i\sin(\omega_m x)\exp(-i\omega_m t)+\mathcal{O}(\epsilon). \qquad (6.32)$$

Equation (6.32) clearly displays leading-order quantities and quantities of $\mathcal{O}(\sigma^2)$ in the $\tilde{u}$ component. Upon further examination, it appears that the infinite power series can be reduced to a more convenient form without loss in accuracy. In fact, since the error associated with $n \geq 1$ terms is smaller than the error at $n = 0$, corrections of $\mathcal{O}(\sigma^2)$ can be retained at $n = 0$ and dismissed in $n \geq 1$ terms. When this is accomplished, an equivalent expression for u_1 is begotten at $\mathcal{O}(M)$. Using the superscript 'U' in reference to the multiple-scale outcome based on the

'undetermined' scaling transformation, we write, in the real domain,

$$u_1^U(x,y,t) = \overbrace{\sin(\omega_m x)\sin(\omega_m t)}^{\text{irrational part}} - \overbrace{\underbrace{F\sin(\omega_m xF)\exp\zeta}_{\text{wave amplitude}}\ \underbrace{\sin(\omega_m t+\Phi)}_{\text{wave propagation}}}^{\text{solenoidal part}} \tag{6.33}$$

where

$$\zeta = \zeta_0 + \zeta_1 = -\xi\eta F^{-3} + 2\xi\sigma^2\eta F^{-2}(F'' + F'^2F^{-1}), \tag{6.34}$$

$$\Phi = \Phi_0 + \Phi_1 = -S\left[\int_0^y F^{-1}(z)dz + 3\xi\sigma^2\eta F^{-3}F'\right]. \tag{6.35}$$

By comparison to u_1^W, u_1^U is slightly more accurate since it reduces to (6.17) when the first-order corrections ζ_1 and Φ_1 are abandoned. A sample comparison between velocity formulations is illustrated in Fig. 3 where numerical and asymptotic predictions are shown to coincide for three different sets of parameters corresponding to $S = 25$, and $K = 10^4$, 10^5 and 10^6. This parametric spread can be achieved, for instance, by reducing the kinematic viscosity by two orders of magnitude while holding constant ω, v_w, and h. Clearly, increasing viscosity promotes shorter penetration depths of rotational waves. In all three cases, the velocity profiles satisfy the no-slip condition at the wall and reduce to the irrotational amplitude along the core. Figure 3 also shows results acquired from numerical simulations of the nonlinear Navier-Stokes equations. Such results were obtained, totally independently, through personal communication [33]. In fact, they were based on the fully implicit, finite volume code described in [34]. The small discrepancies between asymptotic and computational data may be attributed to the finite space and time discretization errors, finite grid resolution, and small Navier-Stokes nonlinearities that escape our analytical formulae.

6.3.6. Other components From the axial component $\tilde{u}$, the normal velocity $\tilde{v}$ can be summoned via mass conservation. To expedite the process, we proceed by setting an ansatz of the form

$$\tilde{v}(x,y,t) = G(y)\cos(\omega_m xF)\exp\zeta\exp[-i(\omega_m t+\Phi)], \tag{6.36}$$

where $G(y)$ is a subsidiary function that must be determined in a manner to satisfy $\partial\tilde{u}/\partial x + \partial\tilde{v}/\partial y = 0$. After some algebra, we find that $G = Mv_0^3$. Henceforth,

$$\tilde{v}(x,y,t) = MF^3\cos(\omega_m xF)\exp\zeta\exp[-i(\omega_m t+\Phi)]. \tag{6.37}$$

Equation (6.37) reconfirms our initial contention that $\tilde{v}/\tilde{u} = \mathcal{O}(M)$. At this point, we may want to present an accurate expression for time-dependent vorticity from the velocity formulation. Indeed, straightforward differentiation begets

$$\tilde{\Omega}(x,y,t) = -S\sin(\omega_m xF)\exp[\zeta - i(\omega_m t+\Phi)]. \tag{6.38}$$

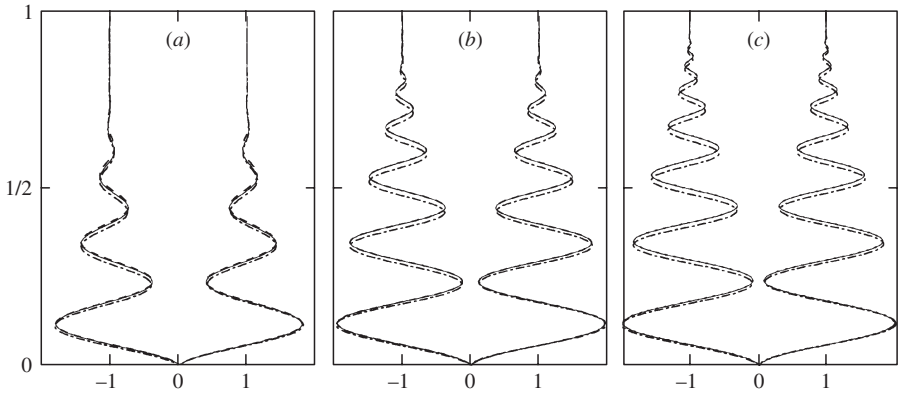

Figure 3.
For the first oscillation modes, we compare profiles of the oscillatory velocity u_1 at two successive times separated by a phase difference of 90 degrees. To the accuracy of the graph asymptotic solutions (full curves) are indistinguishable from numerical simulations of the linearized momentum equation (broken curves). Additional numerical computations of the nonlinear Navier-Stokes equation (chain curves) are shown as well. Here $S = 25$, $x/l = 1/2$, and $m = 1$. Nonlinear finite-volume computations rely on a 400×300 mesh resolution. They are shown after nine iteration cycles for (a) $K = 10^4$, (b) $K = 10^5$, and (c) $K = 10^6$.

The total time-dependent fluctuations can now be expressed, in the real domain, by

$$v_1^U(x, y, t) = MF^3 \cos(\omega_m x F) \exp\zeta \cos(\omega_m t + \Phi), \tag{6.39}$$

$$\Omega_1^U = -S \sin(\omega_m x F) \exp\zeta \cos(\omega_m t + \Phi). \tag{6.40}$$

Despite their disparate formulations, the current expression for vorticity can be shown to coincide with its counterpart in section 5.9. At the outset, it is reassuring to find that the exponential decay of temporal vorticity is decreed by the same agents irrespective of the perturbation technique.

7. Discussion

7.1. The oscillatory wave character

Equation (6.33) represents a travelling wave that begins at the wall and decays in the vicinity of the core. Near the wall, both irrotational and solenoidal amplitudes can couple to produce an overshoot of about twice the irrotational core amplitude. This phenomenon is sometimes referred to as the Richardson velocity overshoot [35] and is common to oscillatory flows. The decaying wave amplitude is a by-product of two mechanisms, viscous dissipation and mean-flow convection. Viscous damping is apparent in the exponential term and is strongly influenced by $\xi =$

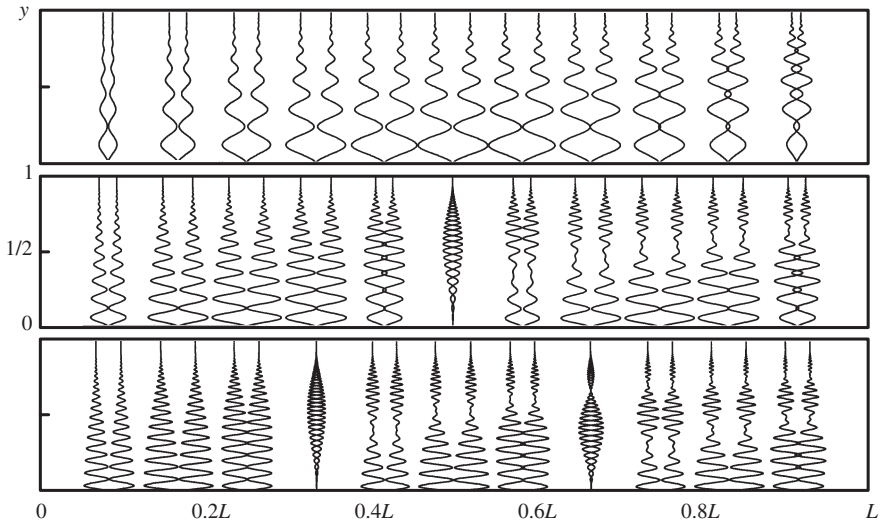

Figure 4.
For the first three oscillation modes, we show profiles of the oscillatory velocity u_1 at two successive times separated by a phase difference of 90 degrees. The profiles are shown at evenly spaced locations within the chamber and correspond to a large injection case with $S = m\pi hL^{-1}M^{-1} = 25m$ and $K = m\pi h^2 a_s L^{-1}\nu^{-1} = 10^6 m$.

$\nu h\omega^2 v_w^{-3}$, $\forall F$. While depreciating with F as $y \to 1$, the convective term varies sinusoidally in the downstream direction. Most of all, (6.33) exhibits a traditional form comprising two distinct components: an inviscid, pressure-driven response, and a viscous, vorticity-driven response. Such constitution is typically associated with oscillatory flows. The reader may consult, for instance, the classic survey by Rott where similar equations are presented for flows over impermeable walls [35]. The current dependence on the axial position can be attributed to the body's finite length. This dependence is not encountered in conventional analyses of oscillatory flows in infinitely long channels.

For a typical test case, the oscillatory velocity is shown in Fig. 4 at equispaced locations within the channel for the first three oscillation modes. Apparently, the rotational amplitude is influenced by the sinusoidal pressure-driven amplitude. Rotational effects are felt deeper as we move downstream due to the mean-flow convection of unsteady vorticity. In fact, lines of zero vorticity that originate at pressure antinodes mark their presence in the velocity profiles while drifting downstream. This explains the m premature decay in the velocity profiles located downstream of the m^{th} internal pressure antinode. Following the premature decay, the rotational amplitude recuperates some strength before resuming its normal depreciation.

Figure 5 illustrates the effect of reducing wall injection by one order of magni-

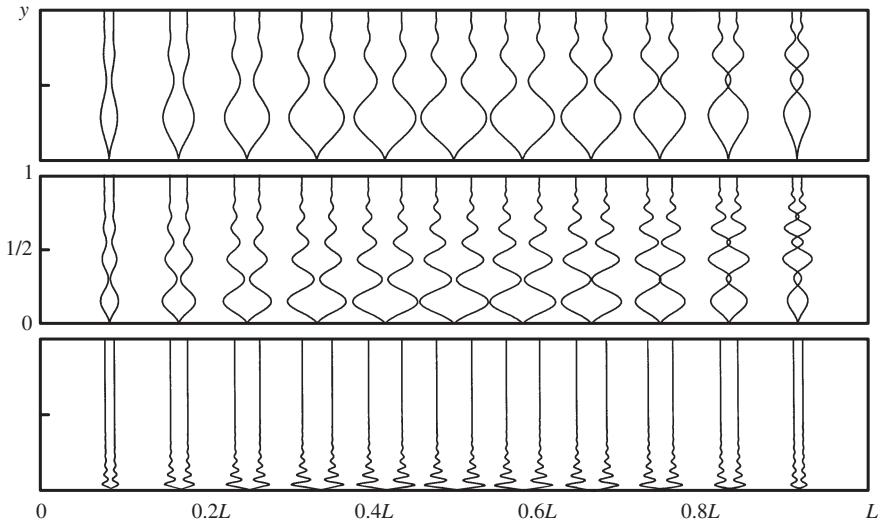

Figure 5.
The effect of varying wall injection is captured by maintaining constant viscosity and frequency, and depreciating the injection at the wall by one order of magnitude. As in the previous figure, we show selectively profiles of u_1 corresponding to $m = 1$, $K = \omega h^2/\nu = 10^5$, and, from top to bottom, $S = \omega h/v_w = 10$, 20, and 100. Clearly, both the rotational wavelength and depth of penetration diminish when wall injection is reduced.

tude. This is accomplished by increasing the Strouhal number while maintaining, at $m = 1$, a constant kinematic Reynolds number. In essence, both the rotational wavelength and depth of penetration diminish when wall injection is suppressed.

7.2. Standard error analysis

Before concluding our discussion, it may be instructive to verify the order of the error associated with the asymptotic formulations, u_1^U, u_1^V, and u_1^C. The latter refers to the multiple-scale solution obtained by substituting η for the composite scale presented in [32]. Following the same procedure described by Bosley [36] and used in [32], we define E_m to be the maximum absolute error between u_1 given asymptotically and u_1^N computed numerically. For example, to determine E_m associated with u_1^U, we calculate over an oscillation cycle,

$$E_m(m, S, \epsilon) = \max_{\substack{0\le x\le l \\ 0\le y\le 1}} |u_1^N(x, y, t, m, S, \epsilon) - u_1^U(x, y, t, m, S, \epsilon)|. \tag{7.1}$$

Assuming a logarithmic error variation of the form

$$E_m(m, S, \epsilon) = \beta(m, S)\epsilon^{\alpha}, \tag{7.2}$$

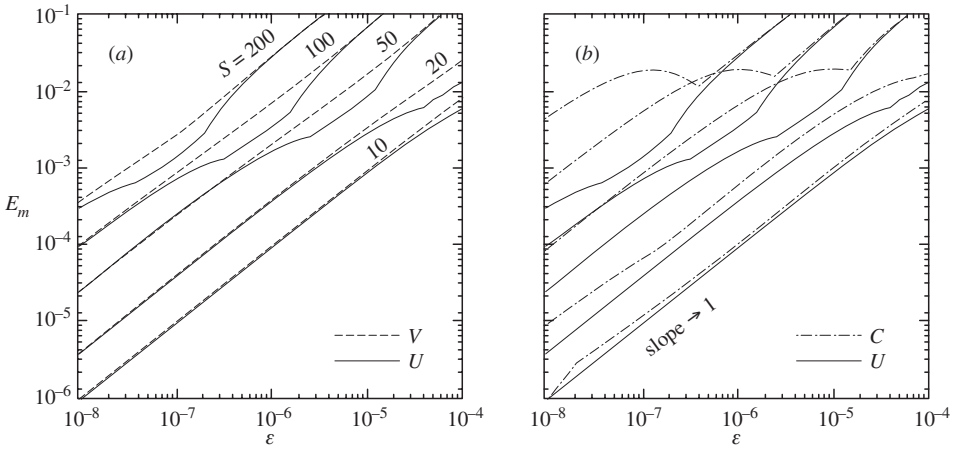

Figure 6.
We compare at $m = 1$ the maximum absolute error entailed in the momentum transport formulation based on the undetermined scale (U) to (a) the vortical transport solution (V), and (b) the solution based on the composite scale (C).

we then evaluate the slope α (representing the order of the error) from the log-log plot of E_m versus ϵ. As borne out in Fig. 6, for all three asymptotic formulations, $\alpha \to 1$ asymptotically regardless of S. The maximum absolute error associated with u_1^U appears to be the smallest. This clear asymptotic behaviour indicates that the error is in fact of $\mathcal{O}(\epsilon)$. Since $\epsilon < M$, the error associated with the asymptotic solutions does not contribute to the overall error of $\mathcal{O}(M)$ entailed in our mathematical model.

8. Concluding remarks

Using three different perturbation schemes, we have developed asymptotic formulations to the oscillatory flow in a channel with wall injection. One formulation was obtained from the vorticity transport equation while the two others were determined from the momentum equation using WKB and multiple-scale expansions. The generalized formulations were derived for an arbitrary mean-flow solution of the Berman type. The asymptotic solutions were shown to agree with one another and with numerical solutions to both linearly perturbed and nonlinear momentum equations. A similarity parameter that controls the rate of viscous damping has appeared in all three formulations. The explicit formulae obtained were useful in revealing (fairly rich) vortical structures caused by mean and time-dependent flow interactions. An absolute error analysis indicated that the two-scale solution based on a nonlinear coordinate transformation was the most accurate. Overall,

the error associated with the asymptotic solutions did not aggravate the error attendant on the mathematical model. The most striking result was, perhaps, the good agreement between asymptotic predictions and numerical simulations of the nonlinear Navier-Stokes equations. Another interesting result is the manner in which the modified coordinate transformation was specified. From a practical standpoint, the generalized solutions we obtained increase our repertoire of useful formulations for periodic flows that occur in a number of engineering applications.

References

[1] A. S. Berman, Laminar flow in channels with porous walls, *J. Appl. Phys.* **24**(9) (1953), 1232-1235.

[2] J. R. Sellars, Laminar flow in channels with porous walls at high suction Reynolds numbers, *J. Appl. Phys.* **26**(4) (1955), 489-490.

[3] G. I. Taylor, Fluid flow in regions bounded by porous surfaces, *Proc. R. Soc. Lond. A* **234** (1199) (1956), 456-475.

[4] S. W. Yuan, Further investigation of laminar flow in channels with porous walls, *J. Appl. Phys.* **27**(3) (1956), 267-269.

[5] M. Morduchow, On laminar flow through a channel or tube with injection: application of method of averages, *Quart. J. Appl. Math.* **14**(4) (1957), 361-368.

[6] F. M. White, Jr., B. F. Barfield and M. J. Goglia, Laminar flow in a uniformly porous channel, *Trans. ASME: J. Appl. Mech. E* **25** (1958), 613-617.

[7] R. M. Terrill, Laminar flow in a uniformly porous channel, *Aeronaut. Q.* **15** (1964), 299-310.

[8] R. M. Terrill, Laminar flow in a uniformly porous channel with large injection, *Aeronaut. Q.* **16** (1965), 323-332.

[9] V. N. Varapaev and V. I. Yagodkin, Flow stability in a channel with porous walls, *Fluid Dyn. (Izv. AN SSSR. MZhG)* **4**(5) (1969), 91-95.

[10] G. D. Raithby and D. C. Knudsen, Hydrodynamic development in a duct with suction and blowing, *Trans. ASME: J. Appl. Mech. E* **41** (1974), 896-902.

[11] J. F. Brady, Flow development in a porous channel or tube, *Phys. Fluids* **27**(5) (1984), 1061-1067.

[12] L. Durlofsky and J. F. Brady, The spatial stability of a class of similarity solutions, *Phys. Fluids* **27**(5) (1984), 1068-1076.

[13] W. A. Robinson, The existence of multiple solutions for the laminar flow in a uniformly porous channel with suction at both walls, *J. Eng. Math.* **10**(1) (1976), 23-40.

[14] F. M. Skalak and C.-Y. Wang, On the nonunique solutions of laminar flow through a porous tube or channel, *SIAM J. Appl. Math.* **34**(3) (1978), 535-544.

[15] K.-G. Shih, On the existence of solutions of an equation arising in the theory of laminar flow in a uniformly porous channel with injection, *SIAM J. Appl. Math.* **47**(3) (1987), 526-533.

[16] S. P. Hastings, C. Lu and A. D. MacGillivray, A boundary value problem with multiple solutions from the theory of laminar flow, *SIAM J. Math. Anal.* **23**(1) (1992), 201-208.

[17] C. Lu, A. D. MacGillivray and S. P. Hastings, Asymptotic behaviour of solutions of a similarity equation for laminar flows in channels with porous walls, *IMA J. Appl. Math.* **49** (1992), 139-162.

[18] A. D. MacGillivray and C. Lu, Asymptotic solution of a laminar flow in a porous channel with large suction: a nonlinear turning point problem, *Meth. Appl. Anal.* **1**(2) (1994), 229-248.

[19] C. Lu, On the asymptotic solution of laminar channel flow with large suction, *SIAM J.*

Math. Anal. **28**(5) (1997), 1113-1134.
[20] M. B. Zaturska, P. G. Drazin and W. H. H. Banks, On the flow of a viscous fluid driven along a channel by suction at porous walls, *Fluid Dyn. Res.* **4**(3) (1988), 151-178.
[21] C. L. Taylor, W. H. H. Banks, M. B. Zaturska and P. G. Drazin, Three-dimensional flow in a porous channel, *Quart. J. Mech. Appl. Math.* **44**(1) (1991), 105-133.
[22] P. Watson, W. H. H. Banks, M. B. Zaturska and P. G. Drazin, Laminar channel flow driven by accelerating walls, *Euro. J. Appl. Math.* **2** (1991), 359-385.
[23] Y. Ma, W. K. Van Moorhem and R. W. Shorthill, Innovative method of investigating the role of turbulence in the velocity coupling phenomenon, *J. Vibration Acoustics-Trans. ASME* **112** (4) (1990), 550-555.
[24] Y. Ma, W. K. Van Moorhem and R. W. Shorthill, Experimental investigation of velocity coupling in combustion instability, *J. Propul. Power* **7**(5) (1991), 692-699.
[25] J. Barron, J. Majdalani and W. K. Van Moorhem, A novel investigation of the oscillatory field over a transpiring surface, *AIAA Paper* 98-2694, 1998.
[26] G. Avalon, G. Casalis and J. Griffond, Flow instabilities and acoustic resonance of channels with wall injection, *AIAA Paper* 98-3218, 1998.
[27] G. Casalis, G. Avalon and J.-P. Pineau, Spatial instability of planar channel flow with fluid injection through porous walls, *Phys. Fluids* **10**(10) (1998), 2558-2568.
[28] M. J. Lighthill, The response of laminar skin friction and heat transfer to fluctuations in the stream velocity, *Proc. R. Soc. Lond. A* **224** (1954), 1-23.
[29] B.-T. Chu and L. S. G. Kovsznay, Non-linear interactions in a viscous heat-conducting compressible gas, *J. Fluid Mech.* **3** (1957), 494-514.
[30] B. T. Carrier and F. D. Carlson, On the propagation of small disturbances in a moving compressible fluid, *Quart. Appl. Math.* **4**(1) (1946), 1-12.
[31] M. Abramowitz and I. A. Stegun, Handbook of Mathematical Functions, National Bureau of Standards 1964.
[32] J. Majdalani, A hybrid multiple scale procedure for boundary layers involving several dissimilar scales, *J. Appl. Math. Phys. (ZAMP)* **49**(6) (1998), 849-868.
[33] T. S. Roh, Private Communication, The California Institute of Technology, 1998.
[34] T. S. Roh, I. S. Tseng and V. Yang, Effects of acoustic oscillations on flame dynamics of homogeneous propellants in rocket motors, *J. Propul. Power* **11**(4) (1995), 640-650.
[35] N. Rott, Theory of time-dependent laminar flows. In: F.K. Moore (Ed.), *High Speed Aerodynamics and Jet Propulsion -Theory of Laminar Flows*, Vol. IV, Princeton University Press, Princeton, New Jersey, 1964, pp. 395-438.
[36] D. L. Bosley, A technique for the numerical verification of asymptotic expansions, *SIAM Rev.* **38**(1) (1996), 128-135.

Joseph Majdalani
Department of Mechanical and Industrial Engineering
Marquette University
Milwaukee WI 53233
USA
(e-mail: maji@marquette.edu)

(Received: December 18, 1997; revised December 5, 1998 and September 9, 1999)